Effect of uncertainties in solar synoptic magnetic flux maps in modeling of solar wind

Alexei A. Pevtsov [a,*], Luca Bertello [b], Peter MacNeice [c]

[a] *National Solar Observatory, 3010 Coronal Loop, Sunspot, NM 88349, USA*
[b] *National Solar Observatory, 950 N. Cherry Avenue Tucson, AZ 85719, USA*
[c] *Space Weather Laboratory, Heliophysics Science Division, Code 674, Building 21, NASA Goddard Space Flight Center, Greenbelt, MD 20771, USA*

Abstract

Recently, the NSO/SOLIS team developed variance (error) maps that represent uncertainties in magnetic flux synoptic charts. These uncertainties are determined by the spatial variances of the magnetic flux distribution from full disk magnetograms that contribute to each bin in the synoptic chart. Here we present a study of the effects of variances on solar wind parameters (wind speed, density, magnetic field, and temperature) derived using the WSA–ENLIL model and ensemble modeling approach. We compare the results of the modeling with near-Earth solar wind magnetic field and plasma data as extracted from NASA/GSFC's OMNI data set. We show that analysis of uncertainties may be useful for understanding the sensitivity of the model predictions to short-term evolution of magnetic field and noise in the synoptic magnetograms.

© 2015 COSPAR. Published by Elsevier Ltd. All rights reserved.

1. Introduction

Synoptic charts of the photospheric magnetic field are the "workhorse" of modern modeling of the solar corona and heliosphere: the charts are used as input to evaluate the topology of magnetic fields in upper solar atmosphere (see, Petrie (2013), and references therein), to predict the shape of the solar corona during solar eclipses (Mikić et al., 2007), and to forecast the solar wind speed near the Earth and throughout the solar system (Arge and Pizzo, 2000). The charts are created by merging together data from a series of full disk observations. In traditional synoptic charts, data from a single full disk image contribute to a selected range of longitudes. Some algorithms combine weighted contributions from several maps to form a selected longitudinal band (Harvey et al., 1980); any changes in a mapped parameter (e.g., magnetic flux) that occur during the period covered by these full disk maps are averaged together. Other algorithms allow producing maps that are constantly updated for the range of longitudes, which are observed on the Earth-side of solar disk (Worden and Harvey, 2000). Until recently, the synoptic charts were treated by the modelers as error-free input. Bertello et al. (2014) developed an algorithm for the creation of uncertainty maps corresponding to the synoptic charts, and investigated the effect of these uncertainties on potential field extrapolations. They found that for typical variances in synoptic maps, the position of open-field areas (coronal holes) and large-scale neutral lines defined by Potential Field Source Surface (PFSS) model may have an uncertainty in its location of about 5° in heliographic coordinates. However, for some topological

---

configurations, the effect on the location of the neutral lines and the coronal holes could be much stronger (Bertello et al., 2014).

To further evaluate the utility of these uncertainty maps, we now employ WSA–ENLIL model (Arge and Pizzo, 2000; Odstrčil et al., 2002) in combination with an ensemble modeling approach. We apply the model to synoptic maps corresponding to periods with different level of solar activity (see, Section 2 for description of our data), and evaluate the level of uncertainty in derived parameters of solar wind resulting from variances in input synoptic maps. Finally, we discuss our findings in Section 3.

2. Data

2.1. Observations of magnetic fields and synoptic charts

Synoptic charts of radial magnetic flux used here are derived using daily full disk longitudinal magnetograms taken with the vector spectromagnetograph (VSM) of the Synoptic Optical Long-term Investigations of the Sun facility (SOLIS; Balasubramaniam and Pevtsov (2011)). The VSM is a full disk spectropolarimeter, which currently takes daily observations of the photosphere (Fe I 630.15–630.25 nm, line-of-sight, LOS and vector magnetograms), chromosphere (Ca II 854.2 nm, LOS magnetograms), and He I 1083.0 nm (maps of equivalent width). The project described in this paper only employs the photospheric LOS magnetograms.

Full-disk magnetograms are sampled at about 1×1 arc-seconds pixels[1] in spatial direction, and they are built by scanning (2048 steps) the image of the Sun by moving the telescope in declination (from terrestrial south to north). It takes about 20 min to complete a full disk LOS magnetogram in Fe I 630.15–630.25 nm. The slit, 2048 pixels in length, is oriented in the (terrestrial) east–west direction; a single scanline provides full spectra for all points on the solar disk from its E to W limb. To compensate for the curvature of the spectrum, SOLIS/VSM implements curved slit with the radius corresponding to about 16,173 arcseconds (the center of the slit is shifted downward (towards terrestrial south) by approximately 32 arcseconds relative to the endpoints of the slit). The image of the slit is split by a focal plane beam-splitter into two equal parts (each 1024 pixels long), and the spectra from each part are re-imaged onto two separate 1024×256 pixel CCD cameras. The LOS magnetograms are derived from the Stokes $(I + V)$ and $(I - V)$ spectra (nominal spectral sampling is 2.3 pm) using the center of gravity algorithm (Rees and Semel, 1979) developed for the NASA/NSO Spectromagnetograph (SPM) operated at NSO/Kitt Peak during 1974–2003 (Jones et al., 1992, 1996). Scanning image by a curved slit results in a non-circular image of the solar disk. This geometric distortion is corrected by shifting image pixels in the scanning direction; the shifts are rounded to the next closest integer pixel (no sub-pixel interpolation). This procedure introduces a slight mis-alignment in the final position of pixels relative to their actual position on solar disk. However, maximum mis-alignment does not exceed half of image pixel (or about 0.5 arcseconds), which is significantly smaller than the typical seeing conditions at the current SOLIS location (about 1–2 arcseconds). As a major advantage, the above procedure is providing full spectral information for each pixel in the geometrically corrected image of the Sun. Gap between two cameras is removed following the procedure described by Marble et al. (2013).

Beginning 2011, an additional step of calibration for modulator inefficiency was added. For a given modulation phase, the efficiency in modulation varies from about 0.96 near the eastern end of the modulator to about 0.75 at the western end (as measured in 2011, see Pietarila et al. (2012)). The time-varying modulator inefficiency function was applied to all VSM data from 2008–present. This correction is applied before the gap removal and the geometric correction steps.

The daily magnetograms have an instrumental offset in zero-point magnetic field (magbias) that varies as a function of pixel position along the slit. This offset is typically within ±2 G (gauss) for the Fe I 630.15 nm line. To remove the magbias, we compute the running flux distribution in 11-pixel-wide vertical bands (parallel to the scanning direction) sequentially shifted by one pixel across the slit. Only pixels with values in the range ±5 G are used. To reduce the effect of large-scale magnetic fields, each band includes all measurements from the last 14 days of observations. Magbias is defined as the center of a Gaussian fit to individual distributions for each vertical band. The magbias is subtracted from the full disk magnetograms prior to the gap-removal and the correction for the geometric distortion.

Next, the individual full-disk magnetograms are re-mapped to heliographic coordinates, which are later combined to create a synoptic chart for a complete solar rotation. Typically, synoptic maps are created for pixels $1° \times 1°$ in size (in solar latitude and longitude). Bertello et al. (2014) proposed using variance of sky-pixels contributing to a single synoptic map pixel as measure of uncertainty for these pixels. While the variance is affected both by the measurements' noise and the statistical properties of the distribution of sky-plane pixels contributing to each synoptic chart pixel, our analysis indicates that the latter has a much larger effect. The reader is referred to our early paper for a detailed description on creating synoptic charts and their corresponding variance maps. Current variance maps (and their archive) for observations taken with VSM/SOLIS can be accessed via SOLIS web site at http://solis.nso.edu/0/vsm/vsm_maps.php.

---

[1] From 2003–2009, VSM used Rockwell cameras with pixel size of 1.125 arcseconds. In 2010, they were replaced by Sarnoff cameras with 1 arcsecond pixel size.

2.2. Data for ensemble modeling

To test the effect of uncertainties on solar wind parameters we selected two Carrington rotations. CR2104 (26 Nov. 2010–23 Dec. 2010) represents period of relatively low sunspot activity with a few small active regions present in the northern hemisphere and only weak dispersed magnetic fields in the South. On the other hand, CR2137 (14 May 2013–10 Jun 2013) corresponds to the rising phase of solar cycle 24 with well-developed active region magnetic field present in both hemispheres. Fig. 1 provides example of synoptic charts of magnetic flux for both Carrington rotations with the corresponding maps of uncertainties. As discussed in Bertello et al. (2014), the uncertainties are larger at the location of strong magnetic fields. The latitudinal distribution of uncertainties follows the distribution of active region magnetic field (active latitudes). The reader may also notice a slight increase in uncertainties towards high latitudes, in the polar regions. The latter is related to the increased level of noise in areas in sky-plane magnetograms situated closer to solar limb (Bertello et al., 2014).

To better demonstrate the significance of the uncertainties (σ), we plot in Fig. 2 the ratio $\sigma/|B_r|$ vs. $|B_r|$ for both pairs of maps shown in Fig. 1. The behavior for both Carrington rotations is very similar. Although the uncertainty σ is in general higher in regions of strong magnetic field, the ratio $\sigma/|B_r|$ shows a strong increase in value with decreasing field strength. This trend is clearly visible up to B_r values of a few Gauss. Regions with larger field strength, up to about 100 Gauss, show a ratio around unity (shown as the horizontal dashed line in Fig. 2). For regions with
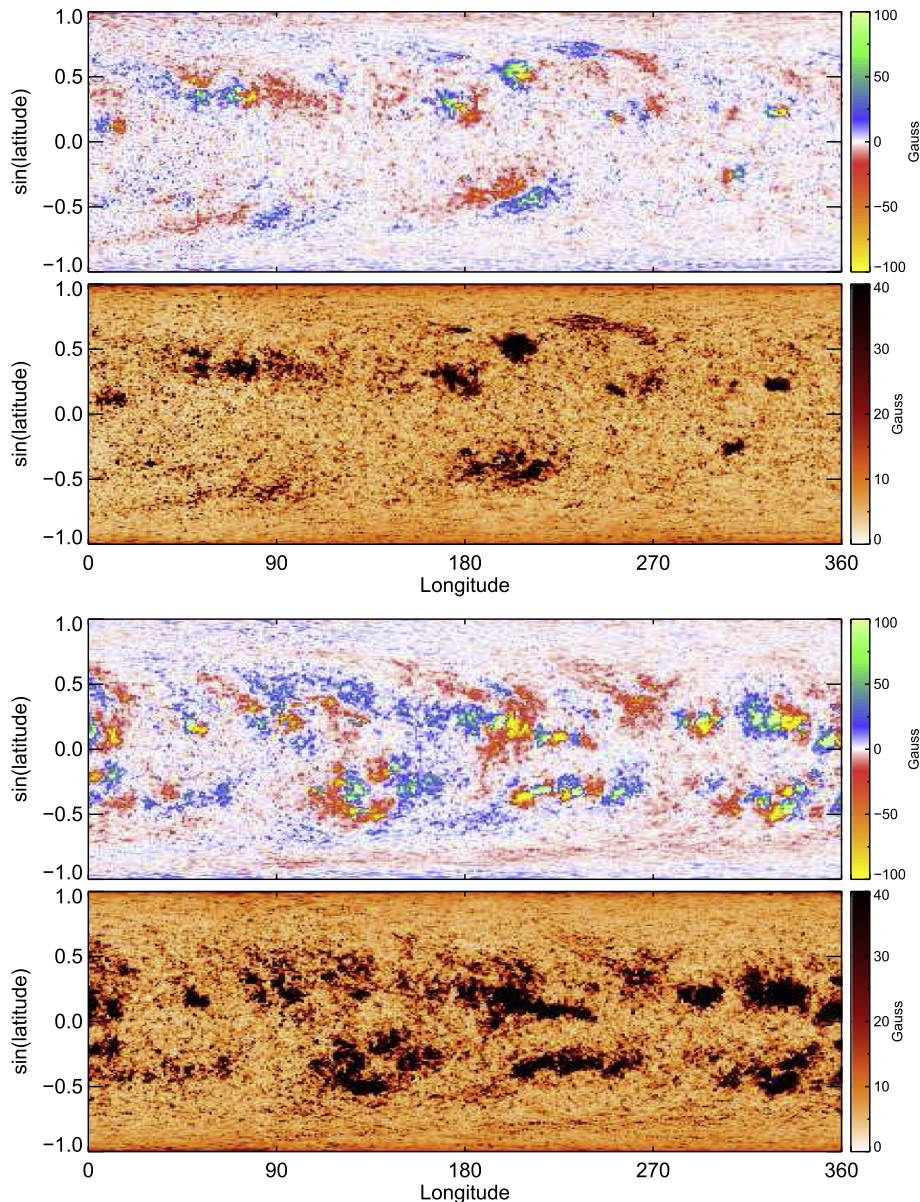

Fig. 1. Synoptic maps of magnetic flux and their uncertainties for CR2104 (two upper panels) and CR2137 (two lower panels).
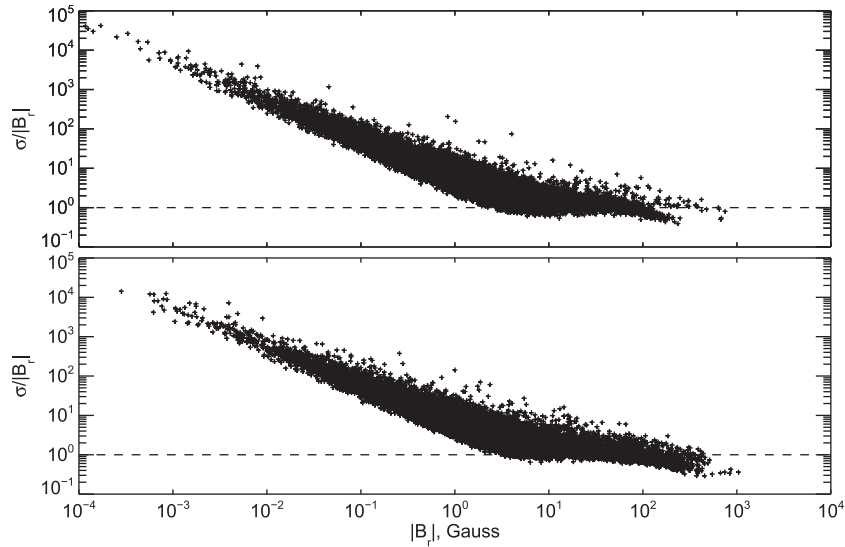
Fig. 2. Relative uncertainty as a function of the radial magnetic field strength for CR2104 (top) and CR2137 (bottom). The horizontal dashed line indicates the boundary $\sigma/|B_r| = 1$.

stronger field strength (above ∼100 Gauss) the ratio tends to be less than one. Flux cancelation plays an important role in determining these trends, as well as the resulting low B_r value at the denominator of the ratio. Typically, several pixels from different magnetograms will contribute to each 1-degree heliographic bin in a synoptic map. When the weighted values of pixels with opposite polarities and covering a broad range in field strength are added together to determine the flux density of that bin, the resulting field strength value could be small but its variance may be large. Fig. 3 shows how the number of pixels contributing to each bin in a synoptic map varies as a function of latitude. For the case of CR2104, 33 different magnetograms were used while this number is 38 for case of CR2137. For both
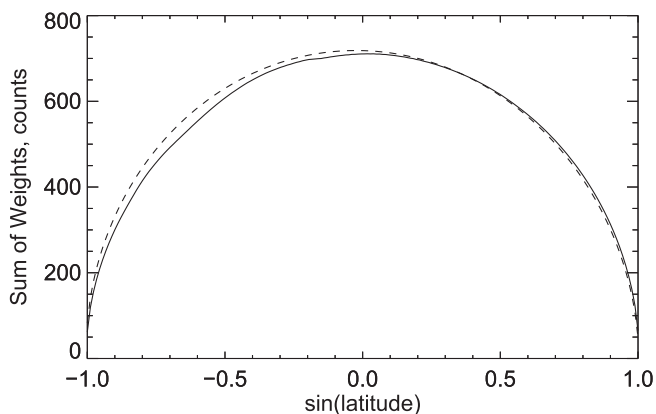
Carrington rotations, the number of sky-plane pixels contributing to 1-degree heliographic pixel reaches almost 700 near the equator and drops significantly towards the polar regions.

2.3. Parameters of WSA–ENLIL model

To evaluate the effect of uncertainties in synoptic flux maps for modeling the solar wind parameters we used the WSA–ENLIL model that runs at the Community Coordinated Modeling Center (CCMC), operated at NASA GSFC. For each of the two Carrington rotations, we created a set of 100 synoptic maps using original synoptic maps of magnetic flux with random uncertainties added. For that test, the uncertainties were generated by a random generator within the range represented by corresponding uncertainty maps derived for each Carrington rotation. In the simulated synoptic maps of the ensemble, the value of each bin is randomly computed from a normal distribution with a mean equal to the magnetic flux value of the original bin and a standard deviation of σ, with σ being the value of the corresponding bin in the uncertainty map. Depending on the particular combination of B_r and σ in the original synoptic map, the polarity of a particular 1-degree bin may be reversed in the randomly generated map. This set of synoptic maps is used to generate ensemble of solutions for solar wind parameters.

The WSA–ENLIL model employed for this study uses WSA V2.2 and ENLIL V2.7. The WSA code rebins the input synoptic maps to a surface grid of size 144 by 72 pixels, uniformly spaced in longitude and latitude with grid cell size of 2.5°. The outer boundary of the current sheet component is placed at 21.5 solar radii (0.1AU). The WSA model computes the solar wind speed (V, in km/s) at 0.1AU using the following formula (McGregor et al., 2011):

Fig. 3. Longitudinal average of weighted contributing pixels as a function of sin(latitude) for CR2104 (solid line) and CR2137 (dashed line). In general, more than a single magnetogram will contribute to the density flux in a 1-degree heliographic bin synoptic map and up to about 200–300 pixels from each magnetogram are averaged together (the number varies slightly during the year with Sun-Earth distance). This number does not change significantly along the longitudinal direction in the synoptic map but, as shown in this plot, has a strong dependency on latitude.

$$V = 240.0 + \frac{675.0}{(1.0 + f)^{\frac{2}{9}}} \times \left[1.0 - 0.8 \cdot exp\left(-\left(\frac{a}{2.8}\right)^{1.25}\right)\right]^{3.0},$$

$$(1)$$

where *f* is the local flux tube expansion factor (i.e., the ratio of the rate of expansion of the local magnetic flux tube compared to that of a purely radial field), and *a* is the angular distance (in degrees) from the photospheric footpoint of the local field line from the closest coronal hole boundary. The WSA solution on this spherical surface is used to provide the inner boundary condition for the ENLIL 3D MHD code. ENLIL uses a grid, uniformly spaced in spherical coordinates, of size 256 by 30 by 90 covering the domain from 0.1 to 2 AU in radius, 30–150° in polar angle (where 0°is the solar north pole), and the full 360° in longitude.

3. Effect of variances for modeling the solar wind parameters

Figs. 4 and 5 compare our modeling results with *in-situ* observations. We chose to compare four main parameters characterizing interplanetary medium: solar wind speed, V_r, proton density N, temperature T, and unsigned magnetic field strength B. For both periods (which corresponds to periods of low and high solar activity), the mean model prediction (green line) agrees relatively well with the average level of observations (red) although for CR2137 there are periods when the average level in model predictions is significantly offset relative to the observed solar wind data. Such offset is more distinct in the proton density (e.g. Fig. 5, days 11–21, and 27–32) and temperature (e.g., days 7–15). The offsets are also present in CR2104 (e.g., Fig. 4, density and temperature panels, days 16–22). Some of these differences may be the result of different level of CME activity, and they may also be caused by the difference in dipolar field of the Sun. Thus, for example, during CR2104, the polar field was still relatively well-defined in both North and the South poles. By CR2137, however, the polar field in the North pole was in the process of its sign reversal, and its polarity was not well defined yet (in fact, polar field was oscillating between positive and negative polarity). The southern pole magnetic field did not reverse its sign yet.

Level of scatter in model predictions (blue lines) varies slightly with time. For example, in Fig. 4 V_r and N (two upper panels) days 25–27 show significantly less scatter in model predictions in comparison with days 14–19. This variability can be related to the longitudinal distribution of uncertainties in CR2104. For example, Fig. 5 in Bertello et al. (2014) shows significant effect of uncertainties on the position of neutral lines in the range of longitudes from 180–270°. The uncertainties in neutral line position in other longitudes are smaller (see, Figs. 4 and 5). Depending on the structure of solar wind, the scatter can vary by a factor of two (temperature and field strength) or even three (solar wind speed and density).

Visually, scatter in velocity and density appears to be higher for CR2104 (c.f. Figs. 4 and 5). Indeed, mean value of standard deviations for 100 model realizations (blue lines in Figs. 4 and 5) from mean model prediction (green line) for solar wind speed, temperature and density are
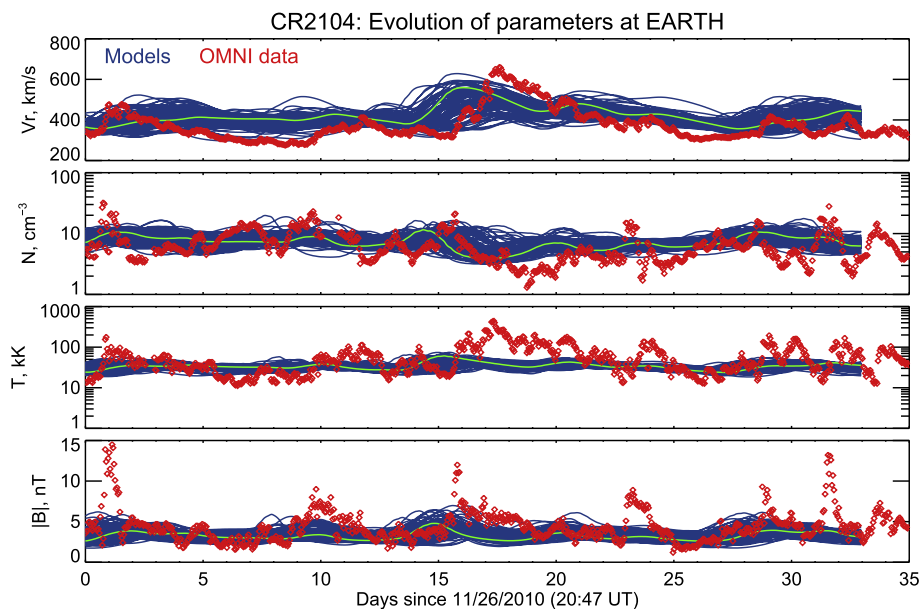

Fig. 4. Evolution of solar wind parameters at Earth computed from the WSA–ENLIL model using a set of 100 Monte Carlo simulation of Carrington synoptic magnetic flux density maps generated from the uncertainty spatial-variance map. Shown here are the results for CR2104. Top to bottom: Radial velocity, proton density, temperature, and magnetic field strength. Observed values (red diamonds) are from the NASA multi-source data set website OMNI. The green solid line is the predicted value from the original magnetic flux density map assuming no uncertainties. (For interpretation of the references to color in this figure legend, the reader is referred to the web version of this article.)
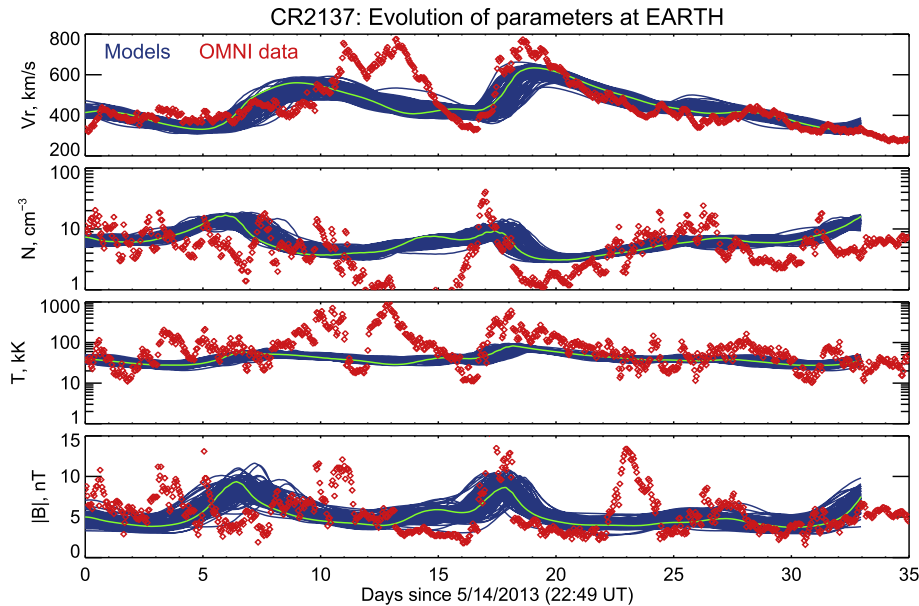
Fig. 5. Same as Fig. 4 but for CR2137.

larger for CR2104 ($\sigma(V_r) = 32.06$ km/s, $\sigma(N) = 1.52$ cm^{-3}, $\sigma(T) = 4.83$ K), as compared with CR2137 ($\sigma(V_r) = 21.63$ km/s, $\sigma(N) = 0.92$ cm^{-3}, $\sigma(T) = 4.38$ K). For magnetic field, scatter in ensemble model predictions is slightly larger for CR2137: $\sigma(|B|) = 0.55$ nT (CR2104) and 0.69 nT (CR2137). This seems to be at odds with the distribution of flux-normalized uncertainties for these two rotations. While the functional dependencies of flux-normalized uncertainties shown in Fig. 2 look similar, CR2104 has a smaller number of points corresponding to stronger magnetic fluxes ($\approx$300–1000 Gauss). The branch corresponding to weak magnetic fluxes (below 1 Gauss) is slightly lower then the branch in CR2137. The latter suggests that for the same amplitude of magnetic flux, the flux-normalized uncertainties in CR2104 are slightly lower than in CR2137. This apparent disagreement demonstrates one of the effects of uncertainties in synoptic maps with different level of activity on model predictions. In CR2104, when the magnetic flux is relatively weak, including uncertainties may result in significant variations and even sign reversal for a mean flux in some pixels of the synoptic map. As the result, the structures in solar wind parameters returned by WSA–ENLIL model may exhibit significant spatial/temporal variations, i.e. small peaks in, say, temperature will be shifted relative to each other in different model realizations, and the overall picture from the ensemble modeling will be less coherent. On the other hand, when the magnetic field is stronger, the uncertainties are less likely to change the sign of magnetic flux of a synoptic map pixel. As the result, the model outcomes from different realizations are more aligned with each other in respect to the peaks and valleys resulting in a lesser scatter in the predicted solar wind parameters.

Observed parameters of solar wind exhibit short-term variations on the order of one day or so. These variations are more prominent in proton density and temperature, but they do present in all four parameters shown in Figs. 4 and 5. The amplitude of these variations is higher during the CR2137. The short-term variations represent small-scale non-uniformities in solar wind, which are not well modeled by kinematic WSA model. In CR2104, the scatter in ensemble solutions is comparable with amplitude of these uncertainties, which masks the deficiency in WSA model to represent these short-term variations.

Variations on longer time scales of about five days (Fig. 5) are indicative of more organized disturbances in solar wind due to fast solar wind streams and coronal mass ejections (CMEs). Some of these structures are represented relatively well (e.g., days 18–25, Fig. 5, upper panel). Other structures (e.g., days 10–17, Fig. 5, upper panel) are not represented by the model at all. Former may be associated with fast solar wind streams originating from the coronal holes, while the latter are likely to be the result of CMEs. Even though the WSA model represents steady structures better than the dynamic ones, the analysis of uncertainties from ensemble modeling suggests that even for these structures, the remaining disagreement between the model and the observations cannot be explained by the uncertainties in the input data.

4. Concluding remarks

We have presented a study of the effects of uncertainties in input synoptic maps of photospheric magnetic flux on solar wind parameters derived using the WSA–ENLIL model and ensemble modeling approach. We argue that this analysis may be useful for understanding the effects of input data on forecasting the solar wind parameters, and for identifying the deficiencies of current models.
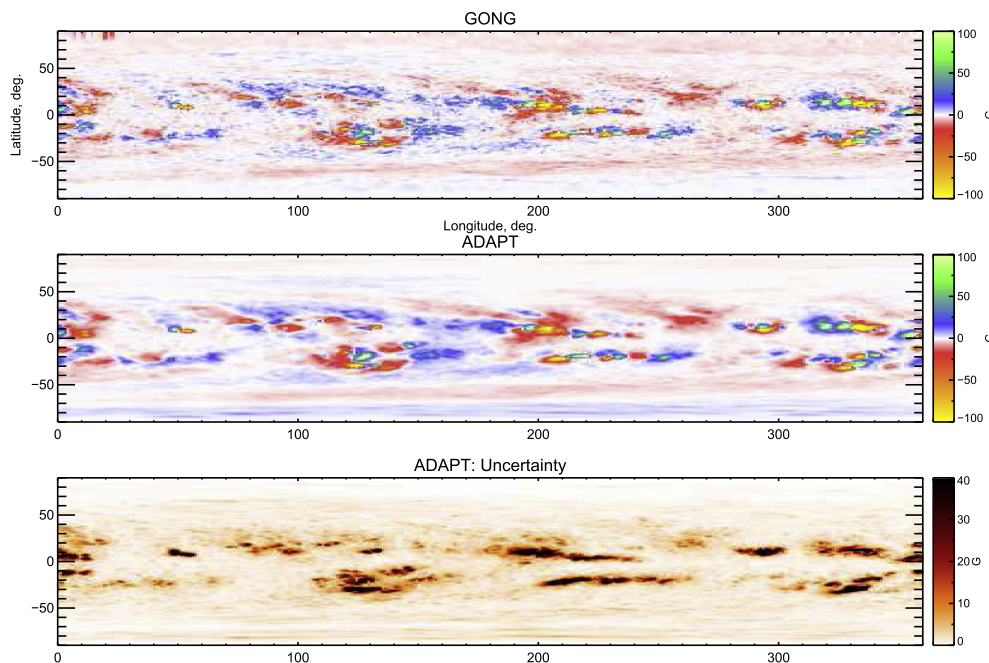
Fig. 6. Comparison between the original CR2137 GONG map (top image) and the one derived from combining several ADAPT maps (middle image). The Pearson's correlation coefficient between the two maps is 0.92, suggesting an overall quite good agreement, with the exception of the polar regions where the two maps are expected to be quite different. The bottom image is the calculated uncertainty on the ADAPT map computed from standard deviation of values from individual dynamic maps contributing to each pixel of integer synoptic map.

It is important to note that the uncertainty maps discussed here represent true uncertainties due to evolution of magnetic fields on the Sun. Although the noise and observation error components are included, they are not the major contributors to the uncertainties. From the description provided in Section 2.2 it follows that one may reduce the level of uncertainties by employing synoptic charts with smaller latitude-longitude bins (e.g., $0.4° \times 0.4°$, instead of traditional $1° \times 1°$ data). While such data do exist (e.g., as one of the SOLIS/VSM current data products), their implementation would require modifying the current WSA–ENLIL model.

One can speculate that using dynamic synoptic maps (that span over adjacent Carrington rotations and are updated every 12–24 h) instead of traditional maps that correspond to integer Carrington rotations may improve the modeling of solar wind and large-scale coronal magnetic field. Recently, a routine production of dynamic synoptic maps started at the National Solar Observatory (NSO) using NSO observations from GONG and VSM/SOLIS. These maps are produced by the Airforce Data Assimilative Photospheric flux Transport (ADAPT) model, and are updated every 12–24 h based on data availability. Fig. 6 shows an example of integer synoptic map for CR2137 constructed from the dynamic synoptic maps produced by the ADAPT model. For this map, the uncertainties were derived from standard deviation of values from individual dynamic maps contributing to each pixel of integer synoptic chars. The uncertainty map constructed from the dynamic maps produced by the ADAPT model is similar to uncertainty maps constructed by our method.

Based on this example, one may expect that the uncertainties in the WSA–ENLIL model prediction based on these dynamic maps will show similar trends as described early in this article. As a continuation of the present study, we are currently investigating the impact of uncertainties when using the dynamic synoptic maps in solar wind prediction. The results of that study will be published in a separate article.

References

Arge, C.N., Pizzo, V.J., 2000. Improvement in the prediction of solar wind conditions using near-real time solar magnetic field updates. J. Geophys. Res. 105, 10465–10480.

Balasubramaniam, K.S., Pevtsov, A., 2011. Ground-based synoptic instrumentation for solar observations. In: Fineschi, S., Fennelly, J. (Eds.) Solar Physics and Space Weather Instrumentation IV, Proc. SPIE, 8148. 814809.

Bertello, L., Pevtsov, A.A., Petrie, G.J.D., Keys, D., 2014. Uncertainties in solar synoptic magnetic flux maps. Sol. Phys. 289, 2419–2431.

Harvey, J., Gillespie, B., Miedaner, P., Slaughter, C., 1980. Synoptic solar magnetic field maps for the interval including Carrington rotation 1601–1680, May 5, 1973–April 26, 1979, report UAG-77. World Data Center A for Solar-Terrestrial Physics, Boulder, CO.

Jones, H.P., 1996. Online analysis and compression of spectra-spectroheliograms. In: Rust, D.M. (Ed). Missions to the Sun, Proc. SPIE, 2804. 110–117.

Jones, H.P., Duvall Jr., T.L., Harvey, J.W., Mahaffey, C.T., Schwitters, J.D., Simmons, J.E., 1992. The NASA/NSO spectromagnetograph. Sol. Phys. 139, 211–232.

Marble, A.R., Callahan, L., Pevtsov, A.A., 2013. Camera Gap Removal in SOLIS/VSM Images, NSO Technical Report No. NSO/NISP-2013-003, 1–9. ArXiv e-prints arXiv:1312.2909.

McGregor, S.L., Hughes, W.J., Arge, C.N., Owens, M.J., Odstrcil, D., 2011. The distribution of solar wind speeds during solar minimum: calibration for numerical solar wind modeling constraints on the source of the slow solar wind. J. Geophys. Res. A 116, A03101.

Mikić, Z., Linker, J.A., Lionello, R., Riley, P., Titov, V., 2007. Predicting the structure of the solar corona for the total solar eclipse of March 29,

2006, solar and stellar physics through eclipses. ASP Conf. Ser. 370, 299–307.

Odstrčil, D., Linker, J.A., Lionello, R., Mikic, Z., Riley, P., Pizzo, V.J., Luhmann, J.G., 2002. Merging of coronal and heliospheric numerical two- dimensional MHD models. J. Geophys. Res. (Space Phys.) 107 (A12) (SSH 14–11).

Petrie, G.J.D., 2013. Solar magnetic activity cycles, coronal potential field models and eruption rates. Astrophys. J. 768, 162–179.

Pietarila, A., Bertello, L., Harvey, J.W., Pevtsov, A.A., 2012. Comparison of ground- and space-based longitudinal magnetograms. Sol. Phys. 282, 91–106.

Rees, D.E., Semel, M.D., 1979. Line formation in an unresolved magnetic element – A test of the centre of gravity method. Astron. Astrophys. 74, 1–5.

Worden, J., Harvey, J., 2000. An evolving synoptic magnetic flux map and implications for the distribution of photospheric magnetic flux. Sol. Phys. 195, 247–268.